The Astrophysical Journal Letters, 878:L36 (7pp), 2019 June 20 https://doi.org/10.3847/2041-8213/ab271d

Effect of Star Rotation Rate on the Characteristics of Energetic Particle Events

Shuai Fu[1,2], Yong Jiang[1], Vladimir Airapetian[3], Junxiang Hu[2], Gang Li[2], and Gary Zank[2]
[1] Institute of Space Weather, Nanjing University of Information Science and Technology, Nanjing, 210044, People's Republic of China
[2] Department of Space Science and CSPAR, University of Alabama in Huntsville, Huntsville, AL, USA; gang.li@uah.edu
[3] NASA Goddard Space Flight Center, MD, USA
Received 2019 March 29; revised 2019 May 30; accepted 2019 June 3; published 2019 June 19

Abstract

The recent detection of superflares on solar-type stars by the *Kepler* mission has raised the possibility that they can be associated with energetic coronal mass ejections (CMEs) and energetic particle events (SEPs). These space weather events can impact the habitability of exoplanets around these stars. Here we use the improved Particle Acceleration and Transport in the Heliosphere (iPATH) model to model the time-intensity profile and spectrum of SEPs accelerated at CME-driven shocks from stars of different ages traced by their rotation rates. We consider a solar-like (G-type) star with six different rotation rates varying from $0.5\Omega_{\odot}$ to $3.0\Omega_{\odot}$. In all six cases, a fast CME is launched with the same speed of $\sim$1500 km s^{-1}; the resulting time-intensity profiles at three locations and energy spectra at five locations at 1 au are obtained. The maximum particle energy at the shock front as a function of r is also shown. Our results suggest that within 0.8 au the maximum particle energy at the shock front increases with the rotation rate of the star. However, event-integrated spectra for the five selected locations along the CME path show complicated patterns. This is because the Parker magnetic field for rapidly rotating stars is more tightly winded. Our results can be used in estimating the radiation environments of terrestrial-type exoplanets around solar-type stars.

Key words: shock waves – stars: rotation – Sun: coronal mass ejections (CMEs)

1. Introduction

White-light solar flares and associated coronal mass ejections (CMEs) are the two most energetic components of space weather affecting the magnetospheric and ionospheric environments of our planet. The energy released in a large eruptive process manifested in an energetic flare and CME can reach up to a few times of 10^{32} erg, and are frequently associated with formation of energetic particles accelerated up to GeV per nucleon (e.g., Zank et al. 2000; Emslie et al. 2004; Mewaldt 2006), producing the so-called Solar Energetic Particle (SEP) events. In large SEP events CMEs and flares often occur together. When the fast CME propagates out, it drives a shock wave and particles are accelerated at the shock front via the diffusive shock acceleration (DSA) mechanism. Because the shocks are spatially extended and the acceleration often lasts over an extended period, accelerated particles can be observed at multiple locations that are longitudinally well separated, and the time-intensity profile of these events are "gradual" in nature. SEPs are commonly regarded as the primary space hazard for astronauts and electric instruments on board spacecraft (Feynman & Gabriel 2000).

A number of authors have modeled SEP events (e.g., Kallenrode 1997; Kóta 2000; Luhmann et al. 2007, 2010; Vainio & Laitinen 2007; Kozarev et al. 2010). One particular model is the Particle Acceleration and Transport in the Heliosphere (PATH) model. The model was originally developed by Zank et al. (2000), who adopted an onion-shell model of the CME-driven shock from which the acceleration and diffusion of energetic particles are followed. This model was improved by Rice et al. (2003), who considered shocks with arbitrary strength, and also by Li et al. (2003), who extended the original PATH model by adding a transport module investigating particle propagation using a Monte-Carlo approach. Li et al. (2005) further extended the model to include the acceleration and transport of energetic heavy ions. These earlier versions of the PATH model are all 1D. Realizing that the shock obliquity is important in deciding the maximum energy at the shock front, Li et al. (2012) attempted to include shock obliquity in the PATH model. However, in the work of Li et al. (2012), the shock obliquity is treated as a fixed parameter and does not vary as the shock propagates out. Therefore, it is still an intrinsic 1D model.

Extending the PATH to a 2D model was accomplished by Hu et al. (2017). The newer version of the model is named iPATH (improved PATH model). Compared to the original PATH model, iPATH has the capability of simultaneously simulating energetic particle time-intensity profiles and spectra at different locations. This is important for understanding observations made by multiple spacecraft of the same event (e.g., Reames et al. 1996; Richardson et al. 2014; Gómez-Herrero et al. 2015). Hu et al. (2018) performed a simulation showing multiple spacecraft observations of the same events. These locations differ in longitudes and heliocentric distances.

Here we apply iPATH to model SEP events forming in the environments of solar-type stars. Young solar-type stars detected by the *Kepler* mission are fast rotators with rotation periods of 3–5 days (Guedel 2007). A significant fraction of these stars (including F-, G-, K-, and M-stars) show superflare events (Maehara et al. 2012). These superflares reach an energy level that is upward of 10^{35} erg and are associated with large starspots occupying up to a few percent of the stellar surface. Solar CMEs are often associated with energetic flares. The relation of fast CMEs can be extended to large superflares observed on young solar-type stars (Alvarado-Gómez et al. 2018). As in the case of solar CMEs, particles can be accelerated to very high energies at the front of these shock waves. These high-energy particles are a major concern of exoplanetary space weather, a subject that has emerged as an important subfield of exoplanetary science and has a crucial

impact on exoplanetary habitability (Airapetian et al. 2016, 2017a, 2019).

The rotation rate of solar-type stars depends on the stellar age, which can vary by a few to a few tens of days. As stars age, they lose angular momentum via magnetized winds (Weber & Davis 1967) and CMEs (Aarnio et al. 2011). Consequently, their rotation rates decrease over time. It is important to investigate how energetic particle environments vary in solar-like stars of various ages and to characterize their effects on exoplanets within close-in habitable zones (HZs) around active stars (Airapetian et al. 2017b). However, such a study requires the knowledge of many stellar space weather environmental parameters. In addition to the stellar rotation rate, one would also need the stellar wind speed, the stellar magnetic field, and the CME speed. Here we focus only on the effect of stellar rotation rate on the resulting energetic particle characteristics, and defer such a study to a later paper.

In this study, we apply the iPATH model as described in Hu et al. (2017). Here we emphasize the importance of shock geometry on the particle acceleration process. The maximum particle energy at the shock front depends on the total diffusion coefficient κ (see Equation (4)) Depending on the rotation rate of the star, the upstream magnetic field can assume different spiral pattern. A faster rotating star will have its spiral magnetic field more winded, while a slower rotating star will have a more radially oriented magnetic field. Consequently, shock geometry can vary significantly for stars of different rotation rates. Therefore, one expects that the shock acceleration process will also be different.

Because the geometry of the Parker spiral field strongly depends on the rotation rate, the geometry of the shock also strongly depends on the star rotation rate. In this Letter, we use the iPATH model to simulate the properties of SEP events from six scenarios of stellar rotation rates relevant to young and old solar-like stars.

2. Model Setup

Denoting $\Omega_\odot$ as the solar rotation rate, we examine six different runs with different rotation rates of $0.5\Omega_\odot$, $1.0\Omega_\odot$, and $1.5\Omega_\odot$, $2.0\Omega_\odot$, $2.5\Omega_\odot$, and $3.0\Omega_\odot$. We model a steady background stellar wind environment in a spherical coordinate system with the background interplanetary magnetic field (IMF) given by a Parker spiral,

$$B_r = B_0\left(\frac{R_0}{r}\right)^2;\ B_\phi = B_r\left(\frac{\Omega r}{u_{\rm sw}}\right)(r \gg R_0). \quad (1)$$

In the above, B_r and B_ϕ are the radial and azimuthal components of the star wind magnetic field at a heliocentric distance r, respectively. Ω is the star's rotation speed, $u_{\rm sw}$ is the star wind speed, and $R_0 = 0.05$ au is the inner boundary. We carry out our simulations on a 2D domain (in the ecliptic plane) with 2000×360 grid points covering a radial range from R_0 to 2.0 au and a longitudinal range from 0° to 360°. The reference location at 0° is arbitrarily chosen. The observer locations are specified relative to this reference location. To investigate the impact of magnetic field geometry on SEP properties, we keep the total magnetic field strength and the stellar wind speed at 1 au as 4 nT and 440 km s^{-1}, respectively. In future follow-up studies, we will apply a self-consistent treatment of the wind speed and the magnetic field that are derived for each stellar age scenario specified by the stellar rotation rate. In all six cases, we set the proton number density and proton temperature at 3800 cm^{-3} and 3.8 MK at the inner boundary, which yield a number density of 5 cm^{-3} and a temperature of 0.04 MK at 1 au, respectively. To simulate a CME-driven shock structure, we perturb the star wind parameters in the inner boundary (0.05 au, $\sim 10R_\odot$) centering at longitude $\phi_c = 100°$. At the center of the CME (corresponding to ϕ_c), the star wind number density and temperature are increased by a factor of 4 and 1.33 from the ambient values and last 1 hr. The magnetic field is not changed at the inner boundary. The initial CME speed profile is taken as a Gaussian form. Denoting the speed at longitude ϕ as $v(\phi)$ we have,

$$v(\phi) = v_0 \exp(-(\phi - \phi_c)^2/\sigma^2), \quad (2)$$

where $v_0 = 1469$ km s^{-1} is the speed at the center and $\sigma = 66.^\circ 6$ is the variance of the Gaussian distribution. Figure 1 is a snapshot of the CME-driven shock for the six different scenarios at $t = 30.2$ hr. As can be seen from the figure, the faster the star rotates, the more twisted the IMF becomes. Points labeled as A, B, and C represent three observers locating at 1 au with longitudes 70°, 100°, and 130°, respectively. The most important information from Figure 1 is that the magnetic connections to the shock front at these three locations vary considerably. Our choices of A, B, and C are such that the shock nose passes point B, and the two flanks pass A and C. The iPATH model used in Hu et al. (2017, 2018) terminates at the shock arrival time, but the newly updated version is capable of simulating the shock arrival and downstream of the shock, therefore including the energetic storm particle (ESP) phase.

3. Simulation Results and Discussion

Figure 2 plots the maximum particle energy and the shock obliquity angle near the shock nose as a function of heliocentric distance. The maximum particle energy is calculated by balancing the shock dynamic timescale $t_{\rm dyn}$ with the particle acceleration timescale $t_{\rm acc}$ (e.g., Drury 1983; Zank et al. 2000),

$$t_{\rm dyn} = \int_{p_0}^{p_{\rm max}} \frac{3s}{s-1}\frac{\kappa}{U_{\rm up}^2}\frac{1}{p}dp. \quad (3)$$

In the above, p_0 is the particle injection momentum, $p_{\rm max}$ is the particle maximum momentum, s is the shock compression ratio, κ is particle's total diffusion coefficient at the shock, and $U_{\rm up}$ is the upstream plasma speed as seen in the shock frame. The total diffusion coefficient κ is related to the parallel diffusion coefficient $\kappa_{||}$ and the perpendicular diffusion coefficient $\kappa_\perp$ and the shock obliquity angle $\theta_{\rm BN}$ through,

$$\kappa = \kappa_{||}\cos^2\theta_{\rm BN} + \kappa_\perp \sin^2\theta_{\rm BN}. \quad (4)$$

The maximum particle energy at the shock front decreases with increasing r as the shock weakens when it propagates out. The green curve is case II (the base case), which is for our Sun. The red curve is case I and corresponds to a star with a rotation speed that is half that of the Sun. We can see that the maximum energy for case I decreases faster than the base case. At 1 au, the maximum particle energy at the shock front for the base case is $\sim$40 MeV/nuc, but $<$30 MeV/nuc for case I. This is

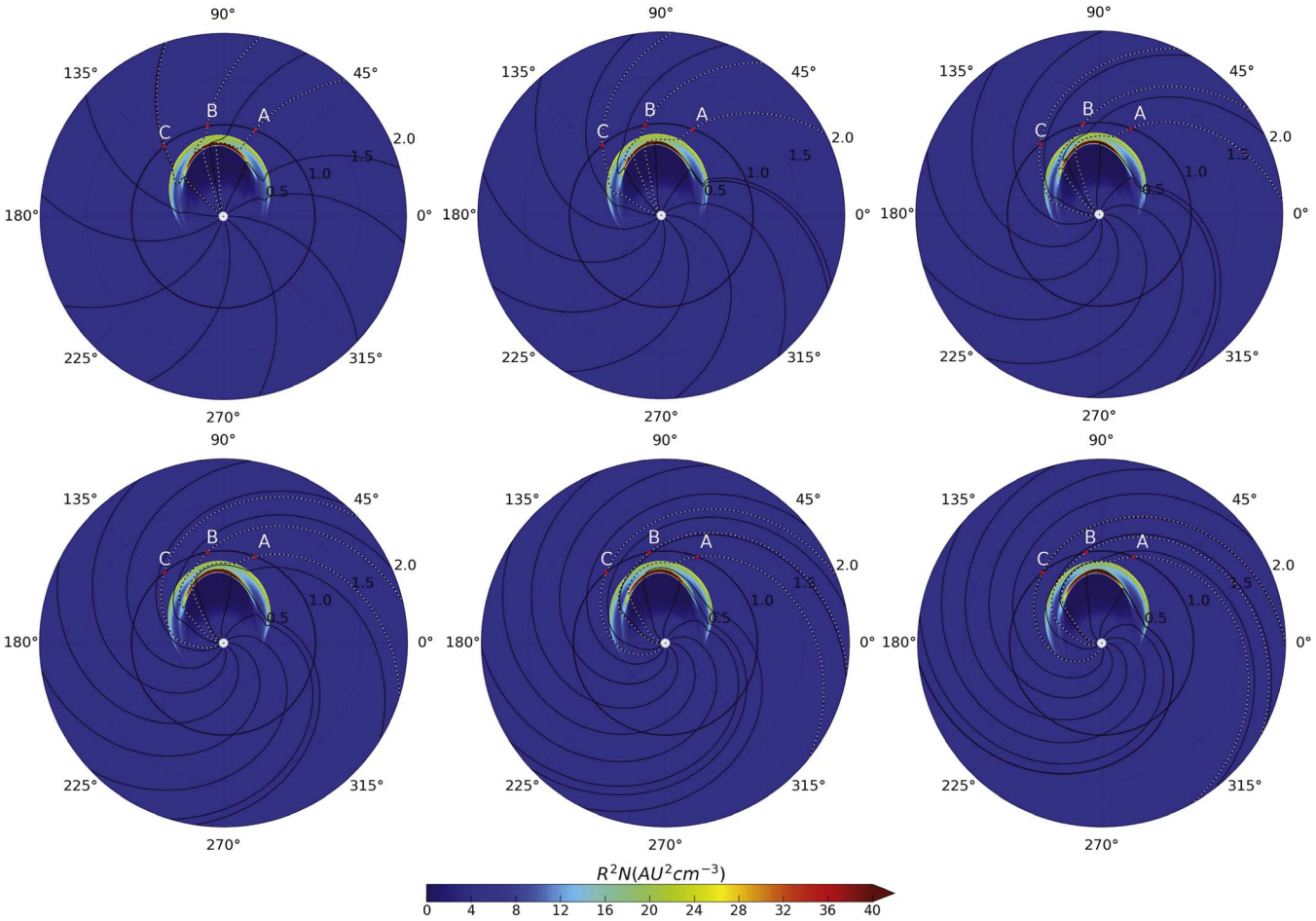

Figure 1. Configuration for the CME-driven shock under six star rotation scenarios at $t = 30.2$ hr after CME eruption. The shock is initiated with the nose toward $\phi = 100°$. The top row, from left to right, shows $\Omega = 0.5\Omega_\odot$ (case I), $1.0\Omega_\odot$ (case II), and $1.5\Omega_\odot$ (case III), respectively; the bottom row, from left to right, shows $\Omega = 2.0\Omega_\odot$ (case IV), $2.5\Omega_\odot$ (case V), and $3.0\Omega_\odot$ (case VI), respectively. In the following, case II is also referred to as the base case. The color scheme is for the normalized density nr^2. The reference points labeled as A, B, and C are located at longitudes of 70°, 100°, and 130°, respectively.

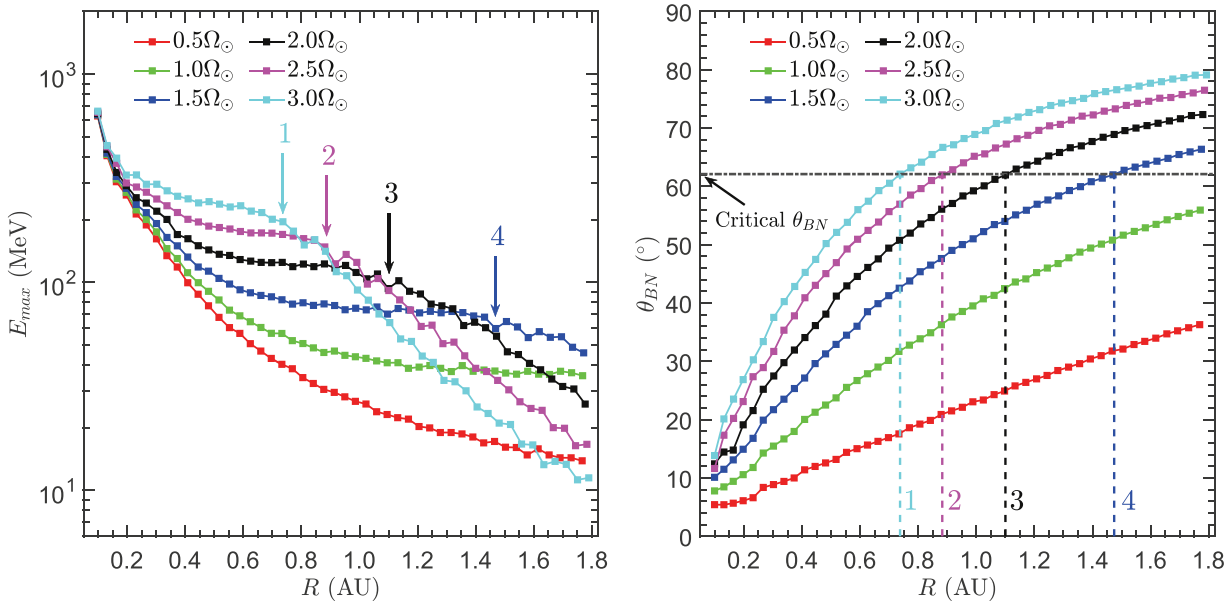

Figure 2. Maximum particle energy (left panel) and the shock obliquity angle (right panel) near the shock nose as a function of heliocentric distance r. The arrow (left panel) and the vertical dashed line (right panel) denote the position where the maximum energy curve falls down substantially. The horizontal dashed–dotted line in the right panel shows the critical value of θ_{BN}.

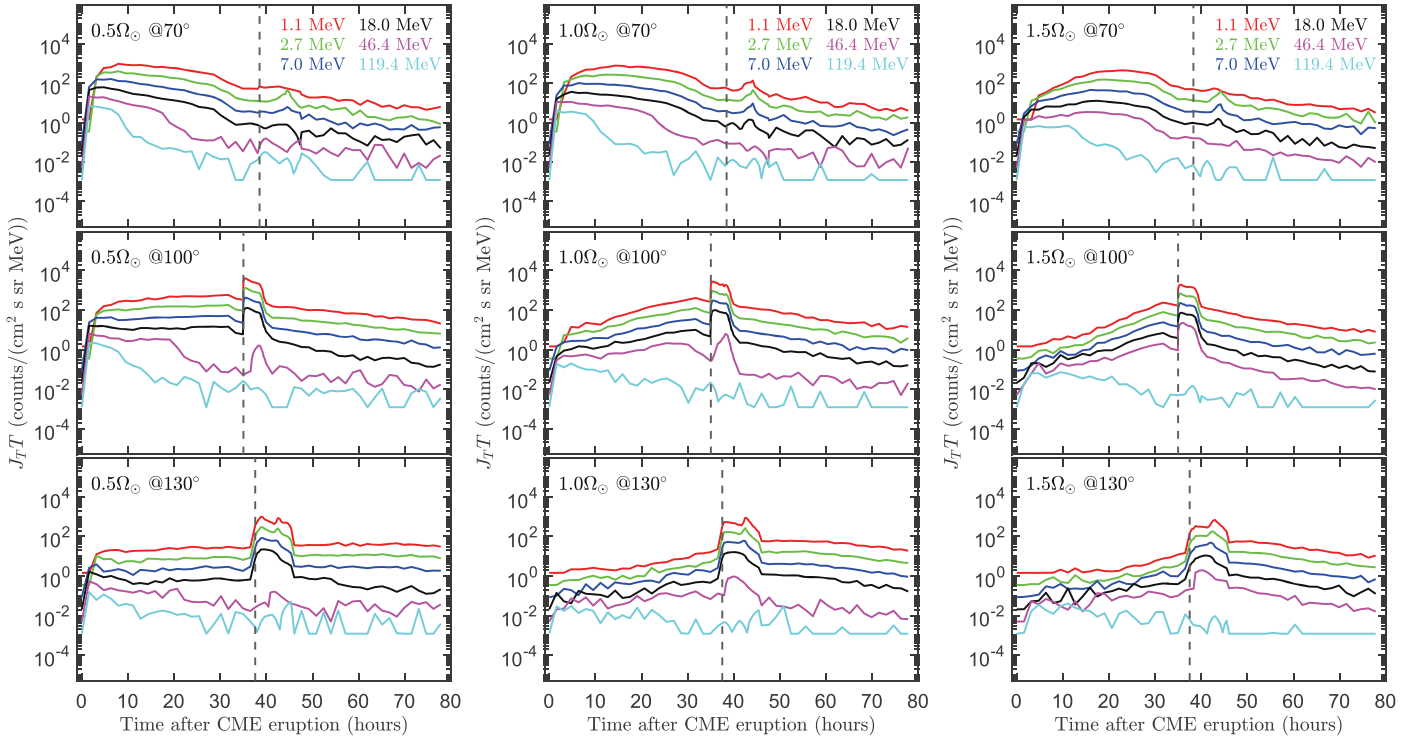

Figure 3. Time intensity profiles for cases I, II, and III. The vertical dashed line in each panel marks the shock arrival time for that reference point.

because the shock in the base case has an obliquity angle that is larger than case I and leads to a smaller total κ at the shock front; from Equation (3), we see that it corresponds to a higher maximum energy. For other cases (case III to case VI), the $E_{\rm max}$ shows an interesting behavior: it quickly drops within ∼0.4 au, followed by a plateau-like period where the $E_{\rm max}$ almost maintains a constant, and then it drops again. The shock nose locations for these drops are: 0.74 au for case VI, 0.88 au for case V, 1.10 au for case IV, and 1.47 au for case III. These locations are marked by the arrows in the left panel of Figure 2. It is interesting to notice that the $\theta_{\rm BN}$'s at these locations are similar. As shown in the right panel of Figure 2, these turning points of $E_{\rm max}$ correspond to a critical obliquity angle $\theta_{\rm BN} = 62°$. One can understand this drop as the following: the total diffusion coefficient, as given by Equation (4), is dominated by the parallel diffusion coefficient $\kappa_{||}$ when $\theta_{\rm BN} < 62°$, and by the perpendicular $\kappa_{\perp}$ when $\theta_{\rm BN} > 62°$. This difference leads to a "break" of $E_{\rm max}$ as a function of r. This can be so because cos$\theta_{\rm BN}$ decreases with increasing $\theta_{\rm BN}$, so the contribution of $\kappa_{||}$ to the total κ decreases with increasing $\theta_{\rm BN}$. It has to be noted that in our model, $\kappa_{\perp}$ is decided by $\kappa_{||}$ through the nonlinear guiding center (NLGC) theory and $\kappa_{||}$ is coupled to the excited waves at the shock front, which in turn is decided by the injection efficiency that depends on $\theta_{\perp}$ itself. How κ varies with $\theta_{\rm BN}$ is therefore nonlinear and it is not straightforward to see how $\kappa_{||}$ or $\kappa_{\perp}$ dominates κ at different values of $\theta_{\rm BN}$. Because of this nonlinear dependence, one should not overemphasize the importance of a critical value of 62° for $\theta_{\rm BN}$. Using a different theory to describe $\kappa_{\rm BN}$, the behavior shown in Figure 2 may vanish. Indeed, the drop of maximum energy for case III (the blue curve) at $r = 1.47$ au is not as rapid as cases IV, V, and VI.

From the left panel of Figure 2, we see that at 0.7 au, $E_{\rm max}$ for case VI is the largest; however, at 1 au, $E_{\rm max}$ for case IV and V are similar and are higher than other cases. At $r = 1.5$ au, $E_{\rm max}$ for case III and IV are similar and are higher than other cases. This of course is the direct consequence of the "break" point occurring at different r's for different cases.

Figure 2 suggests that the stellar rotation rate can affect planetary radiation environments via the fluence of high-energy particles. The maximum energy acquired by the accelerated particles depends on a number of parameters including shock speed, shock compression ratio, and shock geometry. From Figure 2 we can see that the particle maximum energy is greatest for solar-like stars with high rotation rates and decreases with the rotation rate. This has an impact on exoplanetary atmospheric environments. For the terrestrial-type exoplanet with Earth-like (1 bar) atmospheric pressure, particles with the energy of 1 GeV/nuc can penetrate to ∼3 km from the ground, while particles at the low end of energy (10 MeV/nuc) will be stopped via collisions with atmospheric species at 70 km, thus having little effect on the chemistry or dosage of ionizing radiation. The high-energy particles (with energy >0.3 GeV) can penetrate into the lower planetary atmospheres (stratosphere–troposphere region) and induce the enhanced ionization required to ignite atmospheric chemistry producing biologically relevant molecules (Airapetian et al. 2019). Moreover, the strength of the planetary magnetic field is also important because the impact of SEP events depends on the fraction of the open magnetospheric field, which can support an efficient penetration of energetic particles into the planetary atmosphere. This fraction of the open field is moderated by the dynamic pressure of the stellar wind and CMEs associated with SEP events. The exoplanets with weaker magnetic fields and lower surface pressure will be more sensitive to lower-energy particle penetration.

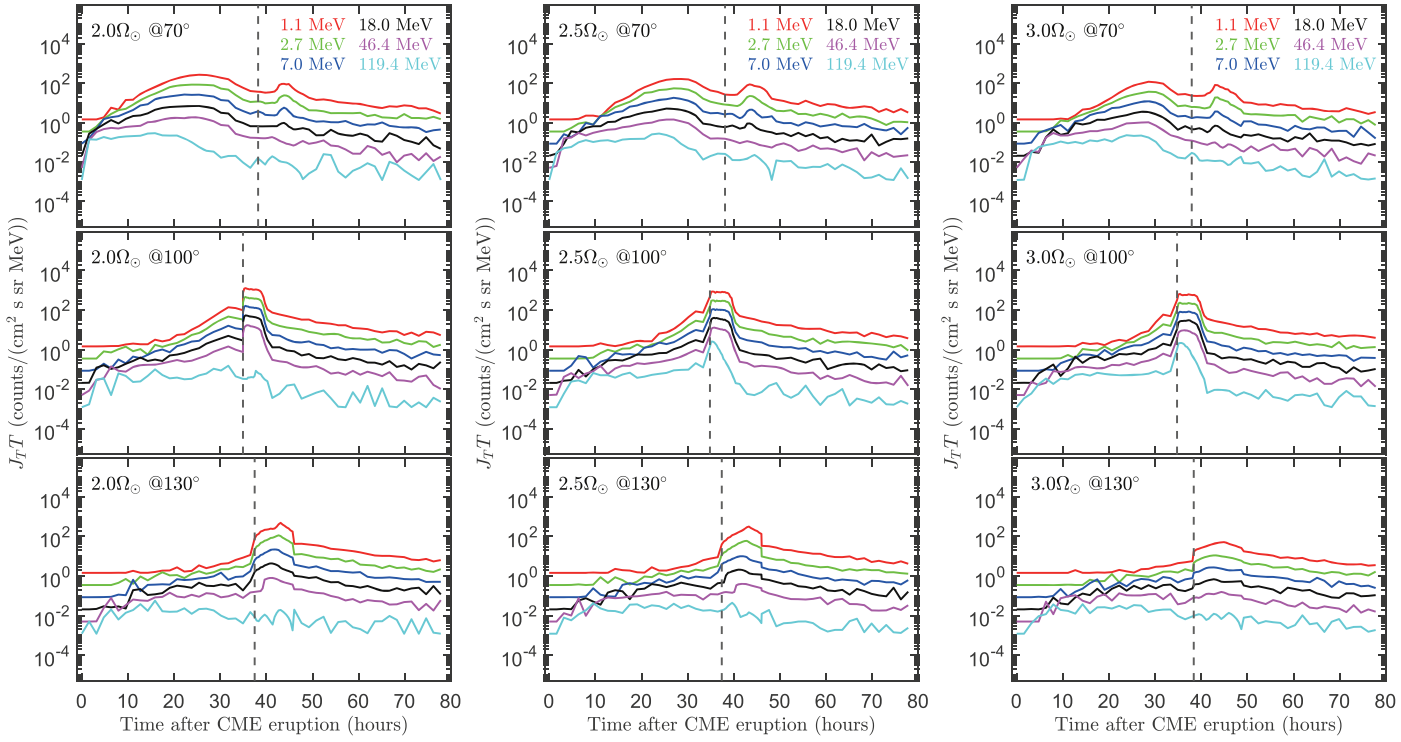

Figure 4. Same as Figure 3 but for cases IV, V, and VI.

In passing, we note that although large SEP events are the greatest hazard during solar maximum, extended exposure to galactic cosmic rays is a greater hazard than SEPs during solar minimum. Indeed, work by Mewaldt et al. (2007) has shown that during solar minimum, fluence of GCR ions dominates that of SEP.

To better understand the radiation environment at the Earth or other planets, time-intensity profiles and particle fluence are necessary. Figure 3 plots the time-intensity profiles for cases I, II, and III. The top panels are for observer A, located at longitude 70°; the middle panels are for observer B, located at longitude 100°; the bottom panels are for observer C, located at longitude 130°. Six energy channels are selected. The vertical dashed line marks the shock arrival. Figure 4 is the same as Figure 3, but for cases IV, V, and VI, respectively. The time-intensity profiles for the same locations but with different rotation rates differ considerably. At point A ($\phi = 70°$), for all energy levels, we can see a fast rise followed by a gradual decay for case I. This is because the shock nose is magnetically connected to the observer at an early time but the connection moves to the eastern flank of the shock as the shock propagates out. For other cases, the rotation rates are faster, so the observers are initially connected to the western flank of the shock. The connections to the shock nose occur at ∼5.0, 16.7, 20.6, 23.0, and 24.6 hr for case II, III, IV, V, and VI, respectively. The rising phase for case III, IV, V, and VI are much slower than case I and a plateau-like period develops. As the shock further propagates out, the connections gradually move to the eastern flank and the intensity profiles begin to decay. In all cases, no clear signatures of ESP phase occur at the shock passage.

For point B ($\phi = 100°$), the time-intensity profiles for all cases are increasing before the shock passes. This is because all observers are connected to the western flank of the shock and gradually move eastward. However, they never connect to the nose of the shock until the shock arrival. In contrast, for point A the ESP phases are very clear in all cases now, and the shapes of the ESP enhancement slightly differ for different rotation rates. After the ESP phases, the intensity profiles begin to decay. For point C ($\phi = 130°$), the observers are connected further to the western flank of the shock and they never connect to the shock nose before shock arrival. Therefore, the initial rises are shallower than for point B. After the shock passes, they begin to decay, but for low-energy channels (1.1–7.0 MeV), they do not decay to a level lower than that before the shock arrival. This is because they are connected to the shock nose where these lower-energy particles are trapped with the shock after the shock passage. The strong longitudinal dependence of the time-intensity profile is the same as reported in Hu et al. (2017, 2018). The inclusion of the ESP phase and its longitudinal dependence is a new feature of the updated iPATH model.

Figure 5 plots the event-integrated spectra at 1 au for 5 locations. From left to right, these correspond to observers at $\phi = 40°$, $\phi = 70°$, $\phi = 100°$, $\phi = 130°$, and $\phi = 160°$. Comparing to the time-intensity profiles shown in Figures 3 and 4, two more observers, at $\phi = 40°$ and at $\phi = 160°$, are added. It can be seen that both the magnitudes and the shapes of the event-integrated spectra vary with observer's longitude and star's rotation rate. Note that for all observers, as the rotation rate of the star increases, the connection to the shock shifts from right to left. This means that an observer at a particular location may not be magnetically connecting to the shock for the whole event. For the observer at $\phi = 40°$, the fluence for the $0.5\Omega_0$ case is the smallest. This is because at the beginning of the event the connection to the shock is already at the right flank.

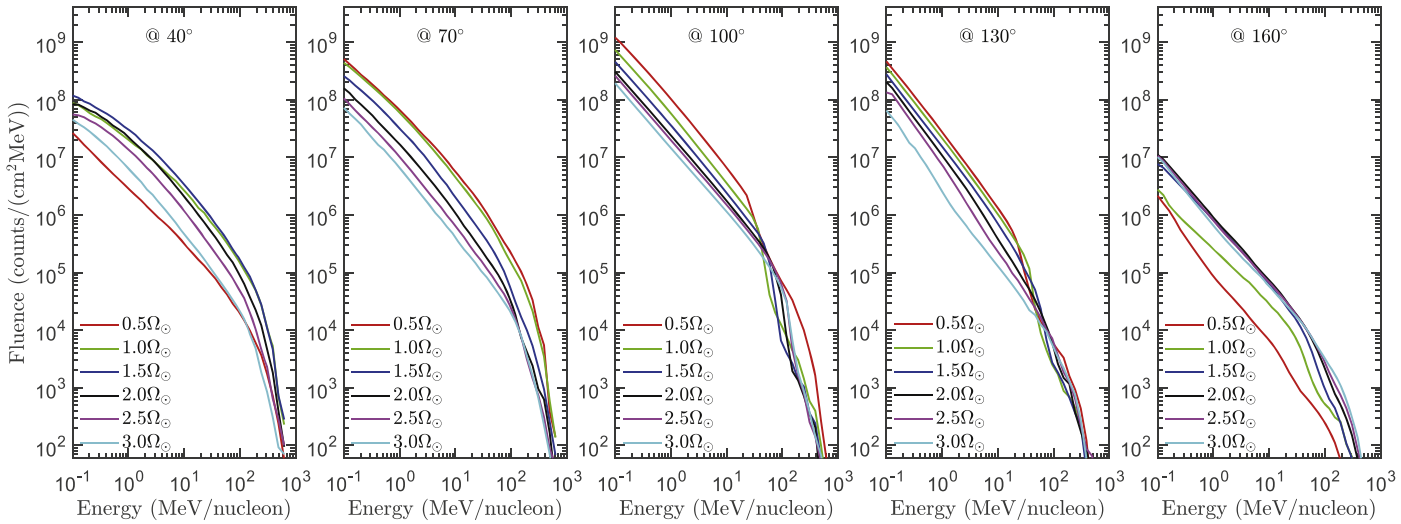

Figure 5. Event-integrated spectra at longitudes of 40°, 70°, 100°, 130°, and 160°, respectively.

As the star rotation rate increases to $1.0\Omega_0$, the connection (at any give time) moves to the left along the shock front, therefore being able to access the shock nose at earlier times where the acceleration is the strongest. When the star rate further increases, however, the connection at early times shifts to the left flank of the shock, where the acceleration is weaker than the case of $1.0\Omega_0$. Consequently, the fluence decreases. For the observer at $\phi = 70°$, the fluence for the $0.5\Omega_0$ and $1.0\Omega_0$ cases are similar and are the largest. Again, this is because in these two cases, the observer has the best connection to the shock (longer duration) compared to other cases. For the observer at $\phi = 100°$, the event is a central Meridian event (because the CME propagates toward $\phi = 100°$). Compared to other longitudes, the fluence at low energy is the largest at $\phi = 100°$. Except for the $0.5\Omega_0$ case, the variations at high energy for different Ωs are small. This is also true for the $\phi = 130°$ cases, where at high energy the fluences for different rotation rates are similar. This is because high-energy particles are accelerated close to the shock; for the observer at $\phi = 130°$, the initial connection to the shock is to the left flank of the shock for all rotation rates, and the accelerated particle spectra at a broad range of the flank do not vary much. The fluence seen at $\phi = 160°$ is interesting. First of all, the fluences for all rotation rates are smaller than those at other ϕ's. This is because the observer at $\phi = 160°$ only connects magnetically to the shock after the shock propagates beyond 1 au. Consequently, almost all particles (except for some that diffuse across fields) observed at $\phi = 160°$ propagate inward from the shock when the shock is beyond 1 au. A faster rotation means that the observer connects to the shock nose at an earlier time. Therefore, the fluence (especially at a higher energy level) is larger for stars with greater rotation rates, as shown in the figure. For the observer locating the nose of the shock (i.e., $\phi = 100°$), clear spectral breaks can be seen. The spectral break energy is related to the maximum energy at the observer location. This can be seen by examining the right panel of Figure 2 with the middle panel of Figure 5, as they correspond to the same longitude. Consider the red curve (case I), the green curve (case II), and the cyan curve (case VI) as examples; their break energies are ∼29.0, ∼38.0, and ∼90.0 MeV, respectively, and the corresponding maximum energy at 1 au is ∼26.7, ∼43.2, and ∼92.5 MeV, respectively.

4. Conclusion and Discussion

In this Letter, we report the results of numerical simulations to examine the effect of star rotation rate on the properties of energetic particles events using the 2D iPATH model. We consider six scenarios for stellar rotation rates ranging from $0.5\Omega_\odot$ to $3.0\Omega_\odot$. Maximum particle energy along the shock front is derived for each of these scenarios. We also model the time-intensity profiles at three locations ($\phi = 70°$, 100°, 130°) and particle spectra at five locations ($\phi = 40°$, 70°, 100°, 130°, 160°). Our results show that the characteristics of SEP events can be affected by the star rotation rate. The rotation rate changes the magnetic connection of the observer to the shock, and alters the shock geometry. The maximum energy gained by a particle at the shock front depends on the shock geometry. The observed time-intensity profiles and event-integrated spectra also depend on the star's rotation rate. However, these dependences on the rotation rate are less prominent at the maximum energy at the shock. This is due to the fact that the shock front is spatially extended, and any given observer over a certain period of time will probe the range of the shock front, leading to a time-intensity profile that is less sensitive to both the longitude and star rotation rate. Because our results show that at high energy the effect of star rotation on the fluence is not significant, they suggest that the variation of star rotation has a limited impact on the atmospheric chemistry of exoplanets with high surface pressure. However, as discussed above, for atmospheric pressures less than 0.5 bar, the impact of SEPs with energy <100 MeV/nuc becomes significant for prebiotic chemistry (Airapetian et al. 2019). On the other hand, the fluence of lower-energy particles have stronger dependence on magnetic field geometry, and therefore the general radiation environment is affected by star's rotation.

Our results provide the first insight into the SEP properties in response to various magnetic field geometries. They form a framework to study stellar SEP events including the fluence, spectra, and maximum energy from stars of different magnetic activity levels that vary over the course of stellar evolution.

Higher level of magnetic activity results in denser and strongly magnetized corona that will drive more energetic flares and CME events. Such energetic CMEs can drive shocks that are lower in the stellar corona than those on the current Sun (Airapetian et al. 2019; Lynch et al. 2019). Our future studies of stellar SEP event will use the results of data-driven magnetohydrodynamic models of evolving solar-like stars based on multi-observatory coordinated observing campaign involving NASA's *Transiting Exoplanets Survey Satellite* (*TESS*), *Hubble Space Telescope* (*HST*), X-ray missions *XMM-Newton*, NICE, and ground-based spectropolarimetry (Airapetian et al. 2019). These studies will be useful in estimating the radiation environment of other Earth-like exoplanets orbiting solar-like stars. This is especially important in light of the upcoming *James Webb Space Telescope* (*JWST*) that will characterize the atmospheric chemistry of exoplanets in the solar neighborhood.

This work is supported at the University of Alabama in Huntsville under NASA grants NNX17AI17G, NNX17AK25G, and 80NSSC19K0075. S.F. and Y.J. acknowledge partial support of National Key R&D Program of China (2018YFC1407304, 2018YFF01013706), Open Fund of Key Laboratory (201801003), and other Foundation (315030409). V.S.A. is supported by NASA grant 80NSSC17K0463, *TESS* Cycle 1 grant 80NSSC19K0381 and GSFC ISFM SEEC grant. S.F. and G.L. acknowledge China University of Geosciences (Beijing) for providing fast and adequate computing resources.

ORCID iDs

Shuai Fu https://orcid.org/0000-0003-4245-3107
Vladimir Airapetian https://orcid.org/0000-0003-4452-0588
Gang Li https://orcid.org/0000-0003-4695-8866
Gary Zank https://orcid.org/0000-0002-4642-6192

References

Aarnio, A. N., Stassun, K. G., Hughes, W. J., & McGregor, S. L. 2011, SoPh, 268, 195
Airapetian, V., Glocer, A., Khazanov, G., et al. 2017a, ApJL, 836, L3
Airapetian, V. S., Barnes, R., Cohen, O., et al. 2019, IJAsB, in press (arXiv:1905.05093)
Airapetian, V. S., Glocer, A., Gronoff, G., Hébrard, E., & Danchi, W. 2016, NatGe, 9, 452
Airapetian, V. S., Jackman, C. H., Mlynczak, M., Danchi, W., & Hunt, L. 2017b, NatSR, 7, 14141
Alvarado-Gómez, J. D., Drake, J. J., Cohen, O., et al. 2018, ApJL, 862, 93
Drury, L. O. 1983, RPPh, 46, 973
Emslie, A. G., Kucharek, H., Dennis, B. R., et al. 2004, JGRA, 109, A10104
Feynman, J., & Gabriel, S. 2000, JGRA, 105, 10543
Gómez-Herrero, R., Dresing, N., Klassen, A., et al. 2015, ApJ, 799, 55
Guedel, M. 2007, LRSP, 4, 3
Hu, J., Li, G., Ao, X., Zank, G. P., & Verkhoglyadova, O. 2017, JGRA, 122, 10938
Hu, J., Li, G., Fu, S., Zank, G., & Ao, X. 2018, ApJL, 854, L19
Kallenrode, M.-B. 1997, JGR, 102, 22347
Kóta, J. 2000, JGR, 105, 2403
Kozarev, K., Schwadron, N. A., Dayeh, M. A., et al. 2010, SpWea, 8, S00E08
Li, G., Shalchi, A., Ao, X., Zank, G., & Verkhoglyadova, O. 2012, AdSpR, 49, 1067
Li, G., Zank, G. P., & Rice, W. K. M. 2003, JGRA, 108, 1082
Li, G., Zank, G. P., & Rice, W. K. M. 2005, JGRA, 110, A06104
Luhmann, J. G., Ledvina, S. A., Krauss-Varban, D., Odstrcil, D., & Riley, P. 2007, AdSpR, 40, 295
Luhmann, J. G., Ledvina, S. A., Odstrcil, D., et al. 2010, AdSpR, 46, 1
Lynch, B. J., Airapetian, V. S., DeVore, C. R., et al. 2019, ApJ, in press (arXiv:1906.03189)
Maehara, H., Shibayama, T., Notsu, S., et al. 2012, Natur, 485, 478
Mewaldt, R. A. 2006, SSRv, 124, 303
Mewaldt, R. A., Cohen, C. M. S., Mason, G. M., Haggerty, D. K., & Desai, M. I. 2007, SSRv, 130, 323
Reames, D. V., Barbier, L. M., & Ng, C. K. 1996, ApJ, 466, 473
Rice, W. K. M., Zank, G. P., & Li, G. 2003, JGRA, 108, 1369
Richardson, I. G., von Rosenvinge, T. T., Cane, H. V., et al. 2014, SoPh, 289, 3059
Vainio, R., & Laitinen, T. 2007, ApJ, 658, 622
Weber, E. J., & Davis, L. 1967, ApJ, 148, 217
Zank, G. P., Rice, W. K. M., & Wu, C. C. 2000, JGR, 105, 25079